



Offshore Sea Levels Measured With an Anchored Spar-Buoy System Using GPS Interferometric Reflectometry

Surui Xie¹ , Jing Chen² , Timothy H. Dixon³ , Robert H. Weisberg² , and Mark A. Zumberge¹ 

¹Scripps Institution of Oceanography, University of California, San Diego, CA, USA, ²College of Marine Science, University of South Florida, St. Petersburg, FL, USA, ³School of Geosciences, University of South Florida, Tampa, FL, USA

Key Points:

- An anchored spar-buoy seafloor geodetic system is used to measure offshore sea levels based on Global Positioning System interferometric reflectometry (GPS-IR)
- Agreement of de-tided daily mean sea levels measured by the GPS spar-buoy and the closest acoustic tide gauge (19.5 km away) is 4.4 cm
- Sea levels measured with the GPS spar-buoy can help improve coastal ocean circulation models

Correspondence to:

S. Xie,
suxie@ucsd.edu

Citation:

Xie, S., Chen, J., Dixon, T. H., Weisberg, R. H., & Zumberge, M. A. (2021). Offshore sea levels measured with an anchored spar-buoy system using GPS interferometric reflectometry. *Journal of Geophysical Research: Oceans*, 126, e2021JC017734. <https://doi.org/10.1029/2021JC017734>

Received 28 JUN 2021
 Accepted 18 OCT 2021

Author Contributions:

Conceptualization: Surui Xie, Timothy H. Dixon, Mark A. Zumberge
Formal analysis: Surui Xie
Funding acquisition: Timothy H. Dixon
Investigation: Surui Xie, Jing Chen
Methodology: Surui Xie
Resources: Timothy H. Dixon
Software: Surui Xie
Visualization: Surui Xie
Writing – original draft: Surui Xie
Writing – review & editing: Jing Chen, Timothy H. Dixon, Robert H. Weisberg, Mark A. Zumberge

Abstract Conventional tide gauges are usually housed along the coast. Satellite altimetry works well in the open ocean but poorly near the coast due to signal contamination by land returns. These limitations lead to an observational gap in the transition zone between the coast and open ocean. Using data collected by a GPS installed on top of an anchored spar-buoy in Tampa Bay, we retrieved water levels through a combination of precise positioning and interferometric reflectometry. Individual water level retrievals agree with a nearby acoustic tide gauge (19.5 km distance) at ~15 cm level. Amplitude and phase of the major tidal constituents are well recovered by the GPS spar-buoy measurements. Over a 2.9-year period, agreement of de-tided daily mean sea levels measured by the GPS spar-buoy and the nearby acoustic tide gauge is 4.4 cm. When sea level data measured by the GPS spar-buoy are included in the local coastal ocean circulation model, low-frequency error propagated from the open boundary is significantly reduced.

Plain Language Summary GPS receivers record direct signals from satellites as well as reflected signals from local objects. The reflected signal can interfere with the direct signal, enhancing or reducing overall signal strength. This characteristic can be used to measure the height difference between the GPS antenna and the reflecting surface. We used GPS data collected by a spar-buoy anchored in Tampa Bay to calculate water levels at different times. The calculated water levels can be used to study sea level change, ocean circulation, and tidal height predictions.

1. Introduction

Coastal sea level exhibits significant spatial and temporal variations, reflecting the influence of tides, winds, coastal currents, varying salinity, and local bathymetry. Measuring, predicting, and understanding these variations in the often densely populated coastal regions are important for a number of economic and natural hazard reasons (Barnard et al., 2015; Hallegatte et al., 2013). Robust measurement of coastal sea level requires both high temporal resolution (e.g., coastal tide gauges and the system described here) and the high spatial resolution afforded by satellites. Pulse-limited satellite radar altimeters have been challenged in coastal areas mainly due to land contaminations. Improved retracking algorithms and new generation altimeters with delay-Doppler/Synthetic Aperture Radar (SAR) mode such as Cryosat-2, Sentinel-3, and Sentinel-6 promise significant advances (International Altimetry Team, 2021), though performance can still be problematic within 5 km of the coast (e.g., Peng & Deng, 2020). Satellite altimetry data require calibration, often performed by comparing to tide gauge observations. However, tide gauge distribution is uneven, may lack simultaneous vertical land motion measurements, and typically does not sample shallow offshore regions. These limitations can affect the calibration, hampering applications of satellite altimetry in coastal waters.

Global navigation satellite systems (GNSS), including the Global Positioning System (GPS), have been widely used in Earth science studies, such as crustal deformation (e.g., Dixon, 1991), atmospheric water vapor variation (e.g., Bevis et al., 1992), ionosphere perturbation (e.g., Ho et al., 1996), tide gauge calibration (Watson et al., 2008), ice motion (Zhang et al., 2008), and volcanic plume detection (Larson, 2013). One of the error sources for precise positioning, multipath, can be used to measure the height and other characteristics of the reflecting surface using a technique called interferometric reflectometry (Karegar et al., 2020; Larson & Nievinski, 2013; Larson et al., 2013, 2017, 2021; Liu & Larson, 2018; Löfgren & Haas, 2014; Peng et al., 2019;

Purnell et al., 2020; Roesler & Larson, 2018; Wang et al., 2020). GNSS interferometric reflectometry (GNSS-IR) exploits the periodic constructive and destructive interference between the direct and the reflected signals. The resulting oscillation in signal-to-noise ratio (SNR) can be used to estimate the height difference between the phase center of the GNSS antenna and the reflecting surface (Larson & Nievinski, 2013). Among different reflectors, water is a nearly specular reflector and is well suited to GNSS-IR applications. Previous studies demonstrated typical root-mean-square (RMS) differences between water levels measured by ground-based GNSS-IR and conventional tide gauges on the order of ~ 10 cm for individual estimates and a few centimeters for daily means (e.g., Larson et al., 2017; Peng et al., 2019; Williams & Nievinski, 2017). When the antenna is in kinematic mode, that is, mounted on a moving platform, water level estimates by GNSS-IR become noisier due to the platform's complicated motion (e.g., Roggenbuck & Reinking, 2019).

Compared to conventional tide gauges (e.g., acoustic sounding tube, radar, or pressure sensors), the sampling rate and corresponding precision for GNSS-IR is lower. However, this technique has several advantages over conventional tide gauges. For example, GNSS-IR can measure absolute water level changes without relying on additional data such as vertical land motion, and the hardware needs little maintenance. Considering that there are many geodetic quality GNSS stations available, and for most of them the primary purpose is precise positioning, GNSS-IR can provide useful sea level measurements with little additional cost.

While water level measurements with GNSS-IR have been demonstrated in a number of studies, previous applications are mainly in coastal areas with stationary GNSS sites (e.g., Larson et al., 2013, 2017, 2021; Peng et al., 2019). Roggenbuck and Reinking (2019) tested the method with three months of data collected by a ship-based GNSS antenna along a ferry route. The standard deviation of the differences between the estimated water levels and a nearby tide gauge measurements in that study was about 4–6 cm. Here, we use a GPS station installed on an anchored spar-buoy to measure offshore water levels at a fixed site in Tampa Bay, Florida (Figure 1). The system was designed for measuring three-component seafloor motion, with the GPS antenna placed on top of the spar, and the bottom of the spar connected to a heavy ballast by a shackle. A float is integrated into the spar to provide buoyancy, keeping the buoy near vertical (Xie et al., 2019). This design is much less expensive compared to construction and deployment of massive rigid spars, and can be redeployed when necessary. The downside is that the GPS antenna is constantly moving due to strong tidal currents and other environmental forcing. These motions are a potential noise source unless appropriate corrections are made. Height changes of the antenna above water reflect a combination of vertical motion of the anchor, spar tilt, and water level changes, although after several months of settling anchor vertical motion is minimal. The system can be deployed in shallow offshore waters, several kilometers or more from the coastline (Xie et al., 2019). Since only GPS data are used in this study, we refer to the method as GPS-IR unless noted.

2. GPS Data

Dual-frequency (L1 and L2) GPS data obtained between August 23, 2018 and July 1, 2021 were used in this study. In different experimental stages, the data sampling intervals differ: 15 s from August 23, 2018 to May 17, 2019, 5 s from May 18, 2019 to August 25, 2019, and 30 s from August 26, 2019 to July 1, 2021. A 17-day data gap occurred between September 16 and October 3, 2020, and the receiver resumed operation after that. However, many short gaps were found in data obtained after October 3, 2020 due to a loose wire contact. A satellite elevation angle mask of 7° was set in the receiver. SNR data collected when the satellite elevation angle was between 7° and 13° were used in the GPS-IR analysis. Figure 1b shows an example of GPS-signal multipath reflection points. Figure 1c shows an example of the sensing zones on water (First Fresnel Zones, see details in Larson & Nievinski, 2013) for satellites at 7° and 13° elevation angles. The gap in the north direction is due to orbit limitations in the satellite constellation. Compared to many coastal GNSS sites where some of the sensing zones are not on water or are obstructed, in our case data collected from all directions can be used.

Some previous GNSS-IR studies used SNR data collected at lower satellite elevation angles (e.g., Larson et al., 2013; Peng et al., 2019; Roggenbuck & Reinking, 2019). In our case, the GPS spar-buoy system was not originally designed for GPS-IR measurements, hence a 7° elevation angle mask was used to reduce multipath noise in precise positioning and limit data rate. A maximum elevation angle of 13° was chosen

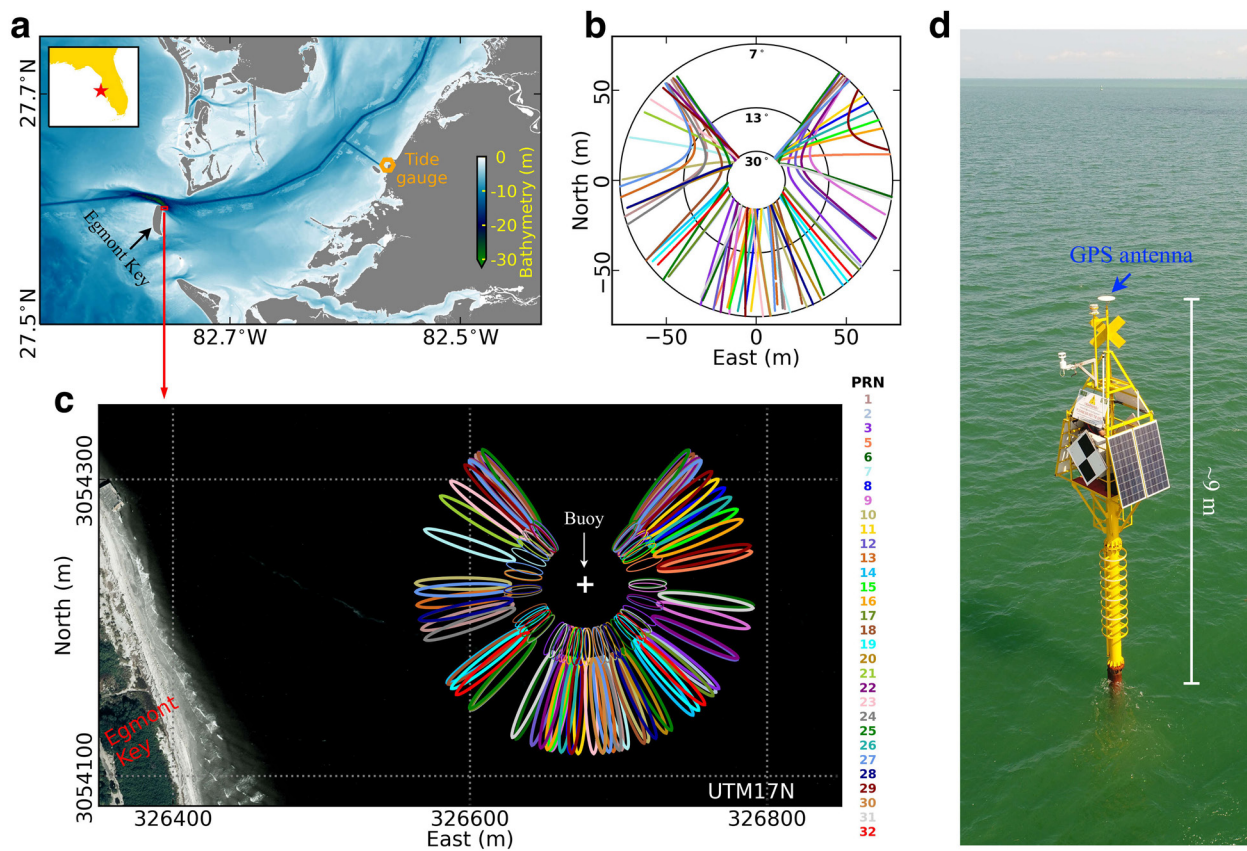


Figure 1. Study area and Global Positioning System (GPS) spar-buoy system. (a) Location of the study area, distance between the buoy and a conventional tide gauge (orange hexagon) is 19.5 km. (b) GPS-signal multipath reflection points on June 6, 2019 when satellite elevation angles are between 7° and 30°, colors correspond to different GPS satellites labeled by pseudorandom noise (PRN) codes in (c). (c) Sensing zones (first Fresnel zones) for satellites at 7° (thick line ellipses) and 13° (thin line ellipses) elevation angles on June 6, 2019. (d) The above-waterline portion of the GPS spar-buoy system.

because the effects of multipath modulation on SNR data become less obvious at higher elevation angles. Nevertheless, a satellite track from 7° to 13° provides enough data for high-quality reflecting height estimates (see below). Figure 2a shows a typical one-day example of satellite tracks used for our GPS-IR measurements.

3. Data Analysis

Water levels are calculated by $H = H_g - H_r$, where H , H_g , and H_r denote water level, elevation of the GPS antenna phase center, and reflecting height (vertical distance between GPS antenna phase center and the water surface), respectively. Kinematic GPS processing to estimate H_g was reported in Xie et al. (2019); we follow the same method here: GPS positions are determined using Precise Point Positioning method provided by the Canadian Spatial Reference System (CSRS, <https://webapp.geod.nrcan.gc.ca/geod/tools-outils/ppp.php?locale>, last access on September 5, 2021). Typical formal error of H_g for a single epoch is 3–5 cm. Gray dots in Figure 3a shows the time series of H_g . An exponential subsidence signal is evident, mainly due to anchor settling and tidal current scouring. The total vertical displacement of the buoy is about -0.9 m during the study period.

To estimate the reflecting height H_r , the method described in Larson et al. (2013) was used, with several changes to account for the motion of the GPS antenna and local water level variation, described in the following steps:

1. Data selection: L1 or L2 data obtained during GPS satellite ascending or descending tracks (7°–13° elevation angle) were analyzed separately. The average satellite transit time of each track is 22 min.

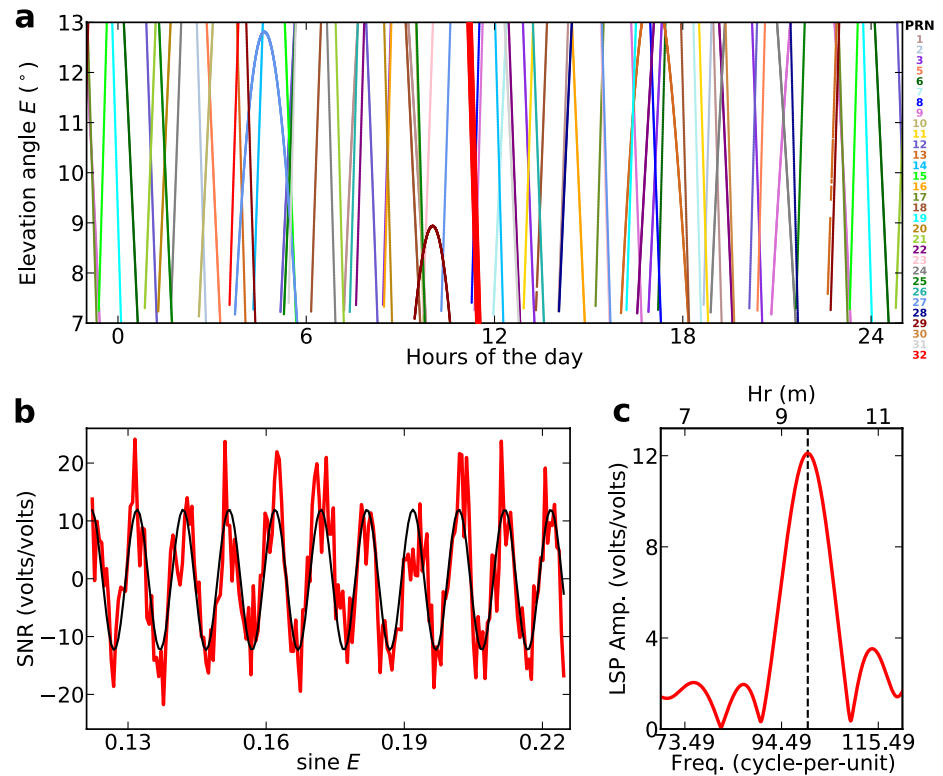


Figure 2. An example of Global Positioning System (GPS) interferometric reflectometry to retrieve water level. (a) GPS satellites observed by the receiver at elevation angles between 7° and 13° on June 6, 2019. (b) Signal-to-noise ratio (SNR) data for the descending track of satellite with pseudorandom noise (PRN) code 32 (marked by the thick red line in a). Red line shows the detrended SNR data, black line shows the least squares fitting of a sine function for the dominant signal. (c) Lomb-Scargle periodogram (LSP) of the detrended SNR data, frequencies are converted to GPS heights above the reflecting surface.

2. Data detrending: A third-order polynomial was used to detrend the SNR versus $\sin E$ data, where E represents the GPS satellite elevation angle. This removes long-period variations due to changes in the receiver-satellite distance and the gain pattern of the antenna, leaving the multipath effect (red line in Figure 2b).
3. Preliminary reflecting height estimate: The dominant frequency of the detrended SNR versus $\sin E$ data was picked by a Lomb-Scargle periodogram (LSP) analysis, which can be converted to preliminary reflecting height using $H_r = \lambda * f_{\max} / 2$, where λ is the wavelength of the GPS signal (19.05 cm for L1, 24.45 cm for L2) and f_{\max} is the dominant frequency picked by the LSP analysis (marked by a dashed line in Figure 2c). For each LSP analysis, a peak-to-noise ratio is calculated as a criterion for quality control.
4. Nonstationary reflecting height correction: Due to tidal variation and buoy deflection, the vertical distance between the antenna and water surface is not constant, biasing the preliminary reflecting height estimate by $\dot{H}_r \tan E / \dot{E}$ (Larson et al., 2013). Two methods were used for the nonstationary reflecting height correction. First, by estimating tidal constituents and using that to derive reflecting height rate. Second, by fitting an eighth-order polynomial for each 3-day time series of H_r and using the derivations of the middle day for corrections. We found that for data with the same minimum LSP peak-to-noise ratio, final water level estimates using the second correction method have smaller discrepancies compared to a nearby tide gauge (Figure 4b). Larson et al. (2013) noted that the first correction method assumed no contribution to \dot{H}_r from influences other than astronomical tides. In our case, the frequently deflected spar (mainly due to wind and ocean current) changed the reflecting height, and there is also frequent meteorological forcing (hurricanes and storms) on local water levels. Hence, we used the second correction method for further analyses. We note that a lower order polynomial is often too smooth, while a higher order polynomial can introduce spurious corrections during extreme weather events.

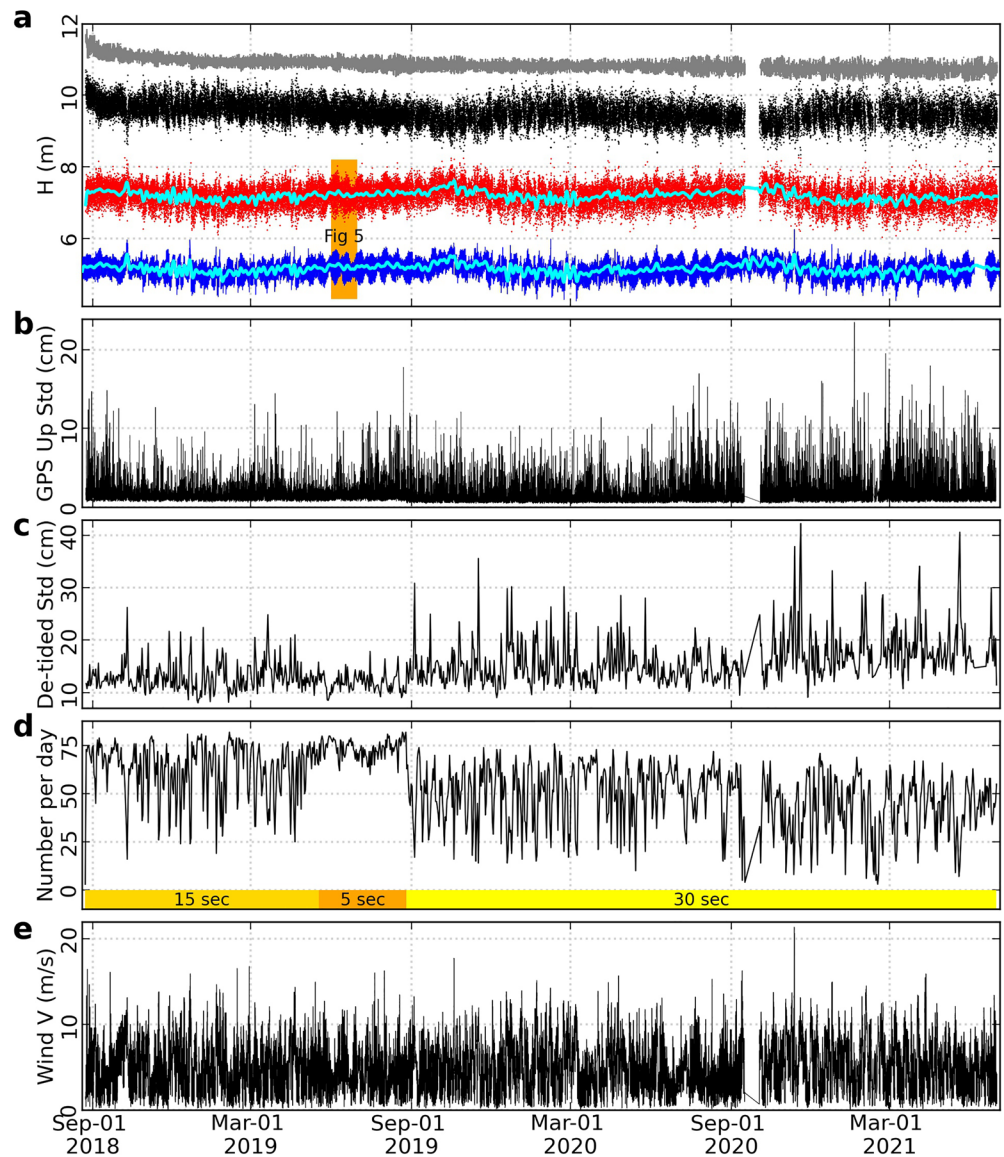


Figure 3. Global Positioning System (GPS) spar-buoy and tide gauge observed water levels. (a) Gray dots show GPS antenna vertical displacements. Black dots show GPS-IR estimated reflecting heights. Red dots show the GPS spar-buoy derived water levels. Blue line shows tide gauge observed water levels (tide gauge location is shown in Figure 1a). Cyan lines show 0.2 cycle-per-day low-frequency-pass filtered water levels. Note except for the black dots, all other markers are offset for clarity. Orange shade marks a one-month period with water levels shown in Figure 5. (b) Standard deviations of GPS vertical displacements over 22-min incremental periods. (c) Daily standard deviations of the differences between de-tided water levels measured by GPS-IR and the tide gauge. (d) Number of water level retrievals per day by GPS-IR, gold, orange, and yellow colors mark periods with different data intervals. (e) Mean wind speed over every 30-min period measured by a wind sensor onboard the spar-buoy. Note the linear correlation between number of water level retrievals per day and daily mean wind speed is -0.70 .

Several criteria were used for quality control. First, an iterative method was applied to ensure that only satellite tracks with observation numbers above the Nyquist sampling limit are used. For example, a preliminary analysis shows that the reflecting heights are between 7 and 11 m during the entire study period, hence a theoretical maximum height of 11.5 m (in a conservative sense) was used to calculate the equivalent frequency and required minimum number of observations to recover the dominant frequency in the subsequent LSP analysis. Second, to ensure the LSP result is robust, the theoretical number of cycles in the SNR versus $\sin E$ must be larger than 3. For example, the satellite track shown in Figure 2b has ~ 10 cycles. Third, to determine if the dominant frequency signal estimated by the LSP analysis is significant, a peak-to-noise

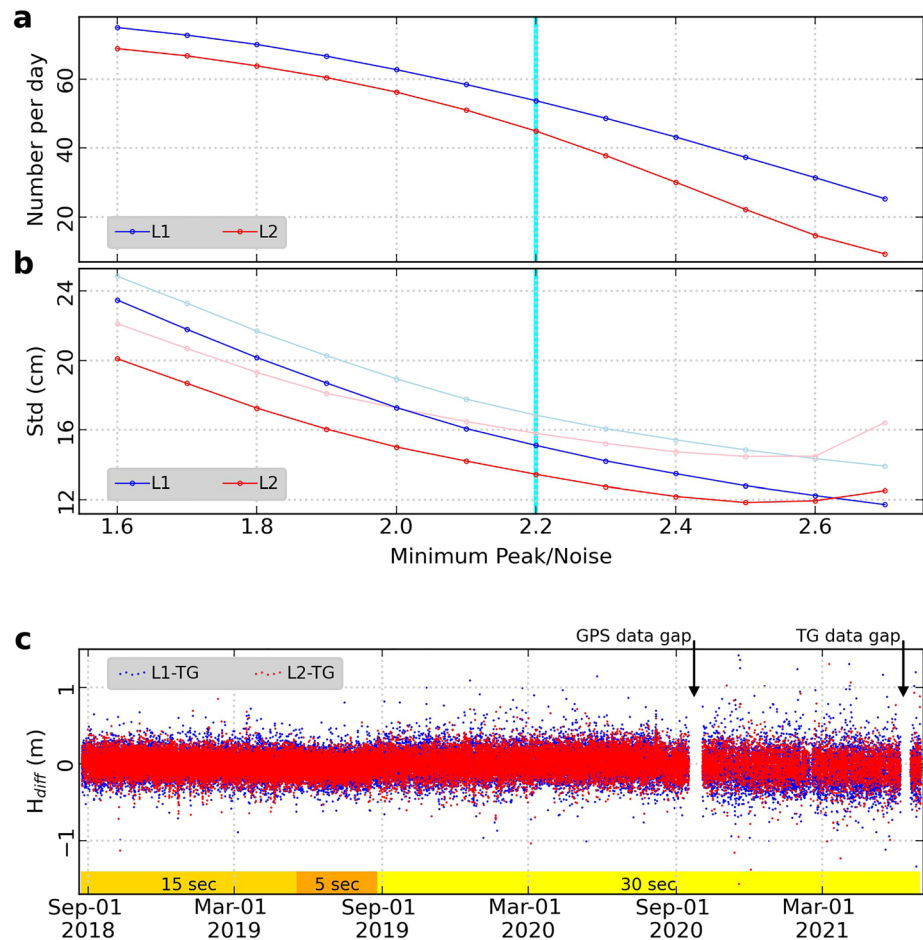


Figure 4. Minimum peak-to-noise ratio of Lomb-Scargle periodogram (LSP) analysis for quality control. (a) Average number of successful reflecting height estimates per day with different peak-to-noise thresholds. (b) Standard deviation of the differences between de-tided water levels at the spar-buoy and the tide gauge. Blue and red dotted lines show results when an eighth-order polynomial was used for reflecting height rate correction (preferred), pink and light blue show results when tidal constituents and reflecting height rate were estimated simultaneously. (c) Differences between de-tided water level measurements at the spar-buoy and the tide gauge. Gold, orange, and yellow colors mark periods with 15, 5, and 30 s data intervals collected by the GPS.

ratio was used as a measure of the data quality for LSP analysis. The background noise band was chosen to be between 6.5 and 11.5 m. This is certainly not the only or the best method to evaluate the significance of a peak in LSP analyzed frequencies (Roesler & Larson, 2018). However, it works well for detecting low quality reflecting height estimates: in general, increased peak-to-noise thresholds correspond to reduced discrepancies between the GPS-IR results and the nearby tide gauge data (Figure 4b). We also found that the average number of water level retrievals per day decreases with increased peak-to-noise threshold (Figure 4a). When the peak-to-noise threshold was set too high, only a small number of water level estimates were kept and many weather events were not represented well in the retrieved water levels. Considering the trade-off between precision and data availability, a minimum peak-to-noise ratio of 2.2 was chosen for the following analyses (marked by cyan line in Figures 4a and 4b).

GPS microwave signals are subject to tropospheric delays and previous work suggests this could perceptibly affect GPS-IR measurements (Williams & Nievinski, 2017). We adopted the correction method of Williams and Nievinski (2017), using the discrete products of the Vienna Mapping Functions 3 (VMF3) and the Global Pressure and Temperature 3 (GPT3) model (Landskron & Böhm, 2018) to calculate the tropospheric delays. While the absolute biases due to tropospheric delays in our GPS-IR reflecting height estimates have a

mean of 11.3 cm, the fluctuation is small, with a standard deviation of 1.2 cm, primarily due to the relatively small tidal range at the study area (~1 m).

Water levels were calculated by subtracting the GPS-IR-measured reflecting heights from GPS-measured antenna phase center elevations. Since both GPS L1 and L2 signals were used, we combined them to form the final water level product. For each satellite track, if both L1 and L2 data retrieve a water level successfully, the weighted mean value was used to define the water level product. Since no ground-truth water levels are available to calculate the weights of L1 and L2 data, and a ~1.5-hr time lag in the major tidal constituents between the buoy and the closest tide gauge prevents direct comparison between GPS-IR results and tide gauge measurements (see below), we weighted L1 and L2 data based on the standard deviations of de-tided water level differences between the GPS-IR and tide gauge data: 15.1 cm for L1 and 13.5 cm for L2 (blue and red dots in Figure 4c). Löfgren and Haas (2014) found that L1 performed better than L2 in GPS-IR water level measurements using SNR data. In our case, under the same quality control criterion, fewer successful water level retrievals were obtained from L2 compared to L1 data. However, L2 retrievals that passed quality control have a slightly better agreement with the nearby tide gauge data compared to L1 retrievals.

4. Discussion

During the study period, an average of 54 water levels per day were retrieved by GPS-IR measurements. While the precision of a single water level estimate by the GPS spar-buoy is much worse than a typical conventional tide gauge (Míguez et al., 2012), it does provide an independent method for sea level monitoring. Below, we discuss quality and potential applications of the water level product derived from the GPS data.

4.1. Factors Affecting the Precision of Water Levels Measured by the GPS Spar-Buoy

Water levels (Red dots in Figure 3a) were calculated by subtracting the GPS-measured reflecting heights (black dots in Figure 3a) from GPS measured antenna phase center elevations (gray dots in Figure 3a). Since the reflecting height estimates are based on LSP analyses of data obtained at different satellite elevation angles, they should be treated as local averages over the corresponding periods (22 min on average). Several factors affect the precision of our water level product, discussed below:

1. Vertical motion of the GPS antenna. Unlike stationary sites on land, the GPS antenna on top of the spar-buoy is constantly moving due to wind and tidal currents. Our previous study shows that on days with moderate sea state, the buoy moves smoothly within a short period (e.g., close to the time length of individual satellite arc for GPS-IR in this study; Figures 5 and 7a in Xie et al., 2019). Hence the nonstationary reflecting height correction works well to address the combined effect of GPS antenna motion and water level change over the satellite tracking period. In contrast, during extreme weather events, tilt and bobbing of the buoy reduces the periodicity of the SNR versus $\sin E$ relation, worsening the precision of the dominant frequency identified by LSP analysis. However, because GPS-IR uses the periodic pattern of the detrended data over tracked satellite arcs for reflecting height estimates, the retrieved water levels are inherently local averages, making it difficult to correct data for individual epochs. Figure 3b shows the standard deviations (Std) of GPS heights over 22-min increments (average satellite arc period). Regardless of the water level changes, if GPS vertical motion varies significantly during the satellite tracking arc periods (e.g., Std > 10 cm), local averages of estimated water levels (calculated by $H = H_g - H_r$) will have larger uncertainties due to increased uncertainties in (H_g). Reducing the spar-buoy cross section or increasing the net buoyancy are possible methods to reduce the influence of buoy tilt and bobbing on GPS-IR water level measurements.
2. Sea state. During the study period, a number of extreme weather events occurred at the spar-buoy site (Xie et al., 2019). Sea state not only affects the GPS antenna motion, but also directly influences the roughness of the reflecting surface. Previous applications of storm surge detections show that high winds downgrade the performance of GNSS-IR for height estimation (Larson et al., 2021; Peng et al., 2019). In our case, during extreme weather events (e.g., hurricanes) fewer satellite tracks fulfilled the quality control and the uncertainty in the sea level estimate is larger compared to days with calm sea state. For example, number of water level retrievals per day (Figure 3d) and daily mean wind speed have a linear

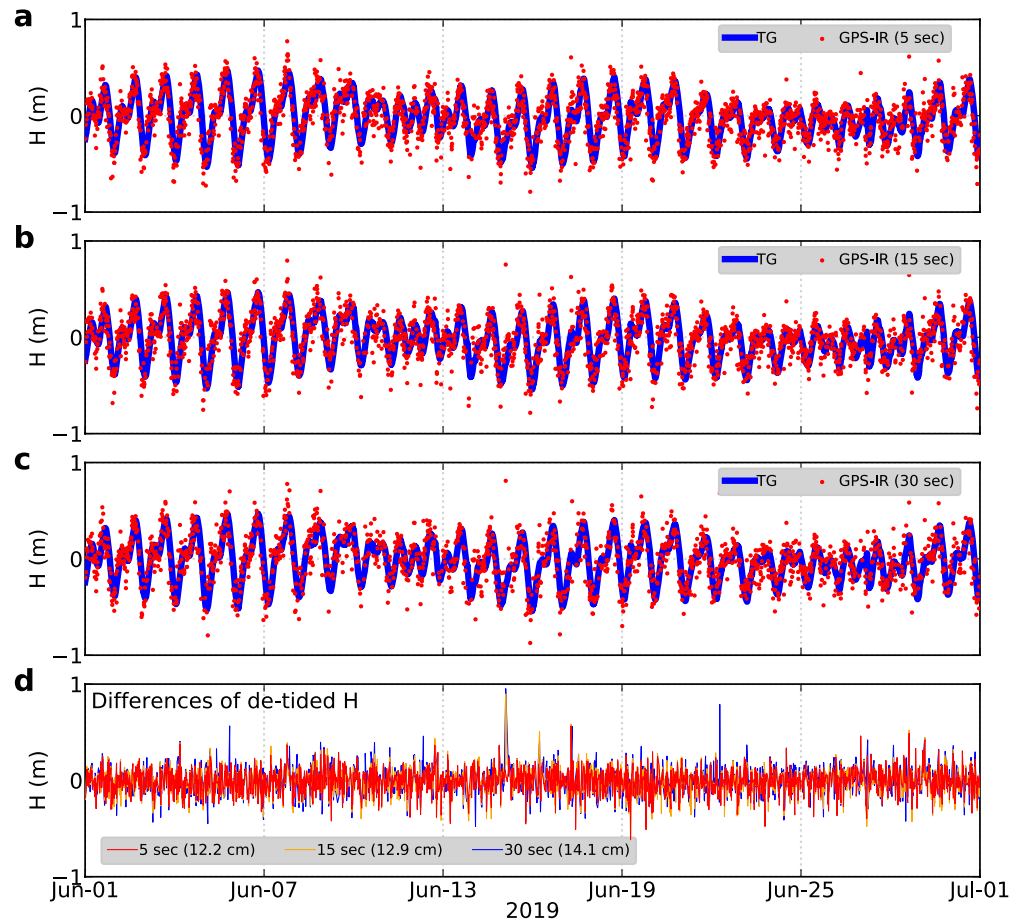


Figure 5. Global Positioning System (GPS) spar-buoy and tide gauge observed water levels (a–c) and the differences (d) for June 2019 (marked by orange shade in Figure 3a). In a–c, blue lines show tide gauge records, red dots show estimates by GPS. 15- and 30-s interval SNR data were down-sampled from 5-s data. All three analyses followed the same quality control. The average number of successful water level retrievals per day are 81, 78, and 71 for 5, 15, and 30-s interval data during the selected month.

correlation of -0.70 , suggesting downgraded performance of GPS-IR during elevated sea states. On the other hand, this suggests the system could be used to measure sea state.

3. GPS data interval. While a Nyquist sampling limit was used for quality control, this criterion only ensures there is just enough observations to estimate a theoretical dominant frequency in LSP analysis. Denser observations allow more precise reflecting height estimates due to increased constraints. Figure 5 compares water levels retrievals with 5, 15, and 30 s interval data in June 2019 (15 and 30 s data were down-sampled from the 5 s data). Higher rate data lead to higher precision in estimated water levels. More importantly, Figures 3d and 5 suggest that higher rate GPS data produce larger numbers of successful reflecting height estimates per day. Therefore, when data storage and transmission allow, higher rate data are preferred.

4.2. Comparison to Conventional Tide Gauge Data

Compared to a conventional coastal tide gauge located 19.5 km away (Figure 1a), precision of water levels measured by the GPS spar-buoy is lower. However, our technique captures both low (cyan lines in Figure 3a) and high (Figure 5) frequency signals well. Figures 6a–6c shows tidal harmonic analyses of water level time series obtained from the two techniques. For the 10 largest tidal constituents, the largest amplitude difference is 1.5 cm. Comparing amplitudes, the differences at the two locations are all smaller than 11% of their amplitudes except for the tidal constituent S1, which has a period of 24 hr that is also the daily

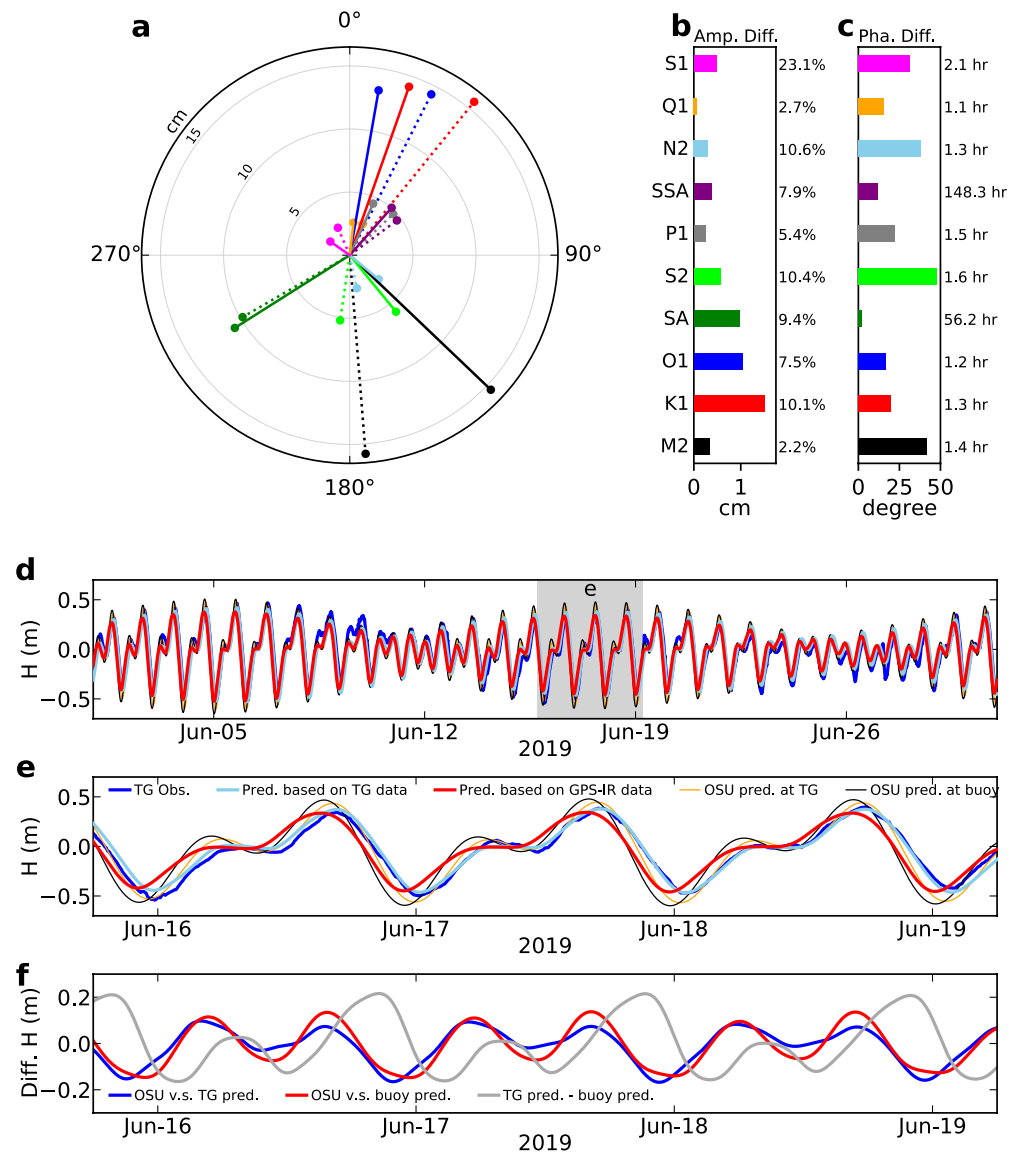


Figure 6. Tidal analyses and predictions. (a) The 10 largest tidal constituents from harmonic analyses of the tide gauge (dotted line) and Global Positioning System (GPS) spar-buoy (solid line) observations, plotted in polar projection. Each color corresponds to a tidal constituent shown in b and c with the same color. (b) Amplitude differences of tidal constituents between the tide gauge and GPS spar-buoy derived results, bottom to top corresponds the largest to smallest tidal constituent (M2 to S1), the right annotations are percentages of the amplitude difference (average of the amplitudes from the two techniques). (c) Phase differences of tidal constituents between the tide gauge and GPS spar-buoy derived results. The corresponding time lags are annotated on the right. (d and e) Water level predictions. Blue line shows tide gauge observed water levels for comparison. (f) Difference in sea level predictions based on observations and model. TG, tide gauge, OSU, OSU TPXO model (Egbert & Erofeeva, 2002). Gray line reflects sea level difference at the tide gauge and buoy locations due to time lag, with a standard deviation of 12.0 cm.

environmental variation cycle. Comparing phases, analyzed tidal constituents at the tide gauge all lag behind the spar-buoy site (Figure 6a). Except for the solar annual and semi-annual terms that have very long periods (8766.2 and 4383.1 hr), the other eight largest tidal constituents have a mean time lag of 1.5 ± 0.3 hr.

Apart from measurement error in the two techniques, the amplitude and phase differences likely reflect true tidal differences at the two locations given the 19.5 km separation. Figure 7 compares the phases and amplitudes of the three largest tidal constituents (M2, K1, O1) derived from the tide gauge measurements, the GPS-IR measurements, and a widely used ocean tide model OSU TPXO (Egbert & Erofeeva, 2002). The

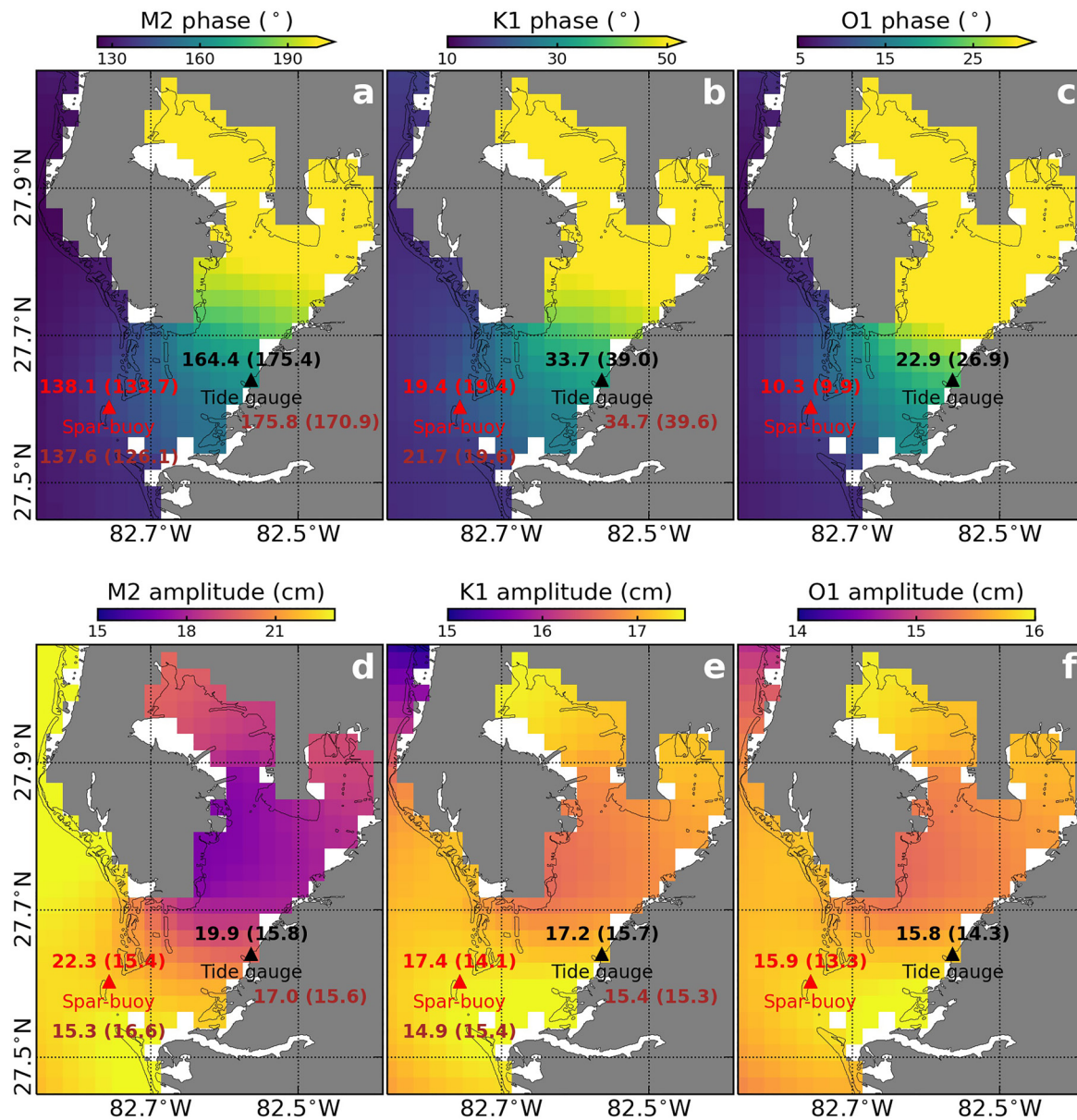


Figure 7. Comparison of phase (top) and amplitude (bottom) of the three largest tidal constituents at the spar-buoy and the tide gauge locations. Color maps show OSU TPXO regional tidal solutions for the Gulf of Mexico. Phase (°) or amplitude (cm) at the spar-buoy or tide gauge location is annotated above corresponding triangle marker, with OSU TPXO modeled value first and then result derived from the GPS spar-buoy or tide gauge observations (in parentheses). For M2 and K1 tidal constituents, text in brown color (under markers) show observed and simulated results from Weisberg and Zheng (2006), with simulated results in parentheses.

ocean tide model shows similar level of amplitude or phase differences at these two locations, though the GPS spar-buoy and tide gauge-derived amplitudes are systematically smaller than the ocean tide model (Figure 7). Weisberg and Zheng (2006) used in situ data and a finite volume coastal ocean model to study Tampa Bay water circulation. They analyzed the principal semi-diurnal, M2, and diurnal, K1, tidal constituents derived from tide gauge data and model simulations (annotated in Figure 7 by cyan text); all match well with our analysis.

To assess the ability of the GPS spar-buoy to monitor sea level change, we subtracted the water level variability due to constituent tides (de-tiding). Figure 8 shows the daily means of de-tided water levels measured by the GPS spar-buoy and two nearby tide gauges. GPS spar-buoy measured sea levels correlate well with tide

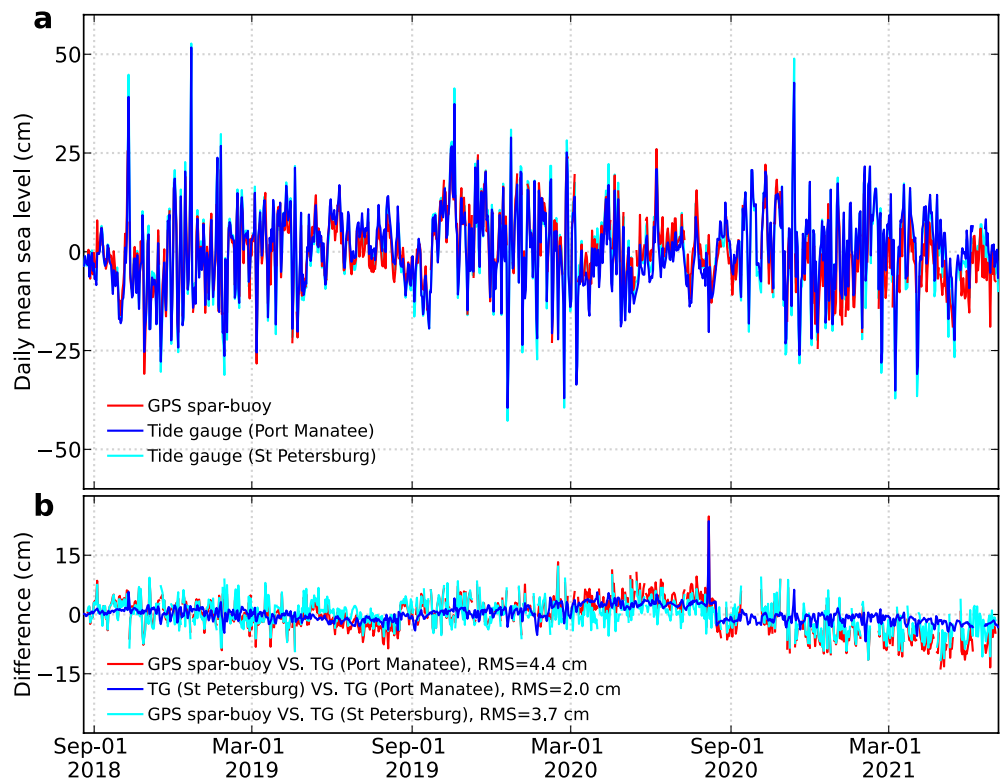


Figure 8. Comparison of de-tided daily mean sea levels measured by the Global Positioning System (GPS) spar-buoy and tide gauges at Port Manatee and St Petersburg (locations shown in Figure 9a).

gauge measurements, with RMS of the differences at 4.4 and 3.7 cm compared to two nearby tide gauges at 19.5 and 21.8 km distances.

4.3. Contribution to Coastal Ocean Modeling

Tampa Bay is the largest of the Florida coastal plain estuaries. With spatial resolution as fine as 20 m, the Tampa Bay Coastal Ocean Model (TBCOM) resolves the channels, inlets, bridge causeways, and other geometric complexities (Chen et al., 2018). To maintain high resolution within the estuary and properly account for exchanges between the continental shelf and estuary, TBCOM downscales from the continental shelf to the estuary by nesting the unstructured grid of the Finite Volume Community Ocean Model (FVCOM) (Chen et al., 2003) in the West Florida Coastal Ocean Model (WFCOM) (Weisberg et al., 2014; Zheng & Weisberg, 2012), which in turn downscales from the deep ocean across the continental shelf by nesting FVCOM in the Gulf of Mexico Hybrid Coordinate Ocean Model (HYCOM) (e.g., Chassignet et al., 2009).

Sea levels observed by tide gauges are important data to validate ocean circulation models. Previously, TBCOM used sea level data obtained at several coastal tide gauges and velocity profiles from a station within the main shipping channel to evaluate the model simulations (Chen et al., 2018, 2019). The veracity of TBCOM was demonstrated by simulating the Tampa Bay circulation as driven by tides, winds and rivers, and reproducing the sea level and circulation under both normal weather conditions (Chen et al., 2019; Zhu et al., 2015) and extreme events such as Hurricane Irma (Chen et al., 2018). Similar misfits of sea levels between lowpass filtered observations and model simulations were found at the tide gauge and GPS spar-buoy locations (Figure 9c). These errors originate both from the open boundary sea levels that propagate to the coastal and estuary areas and errors in the local winds used to force the model (e.g., He et al., 2004; Mayer et al., 2017). Because the misfit at our GPS spar-buoy station is at a similar level compared to the conventional tide gauges, data obtained by the GPS spar-buoy can be used to adjust the model simulations with similar accuracy compared to a conventional tide gauge. Table 1 lists the correlation coefficients (CCs)

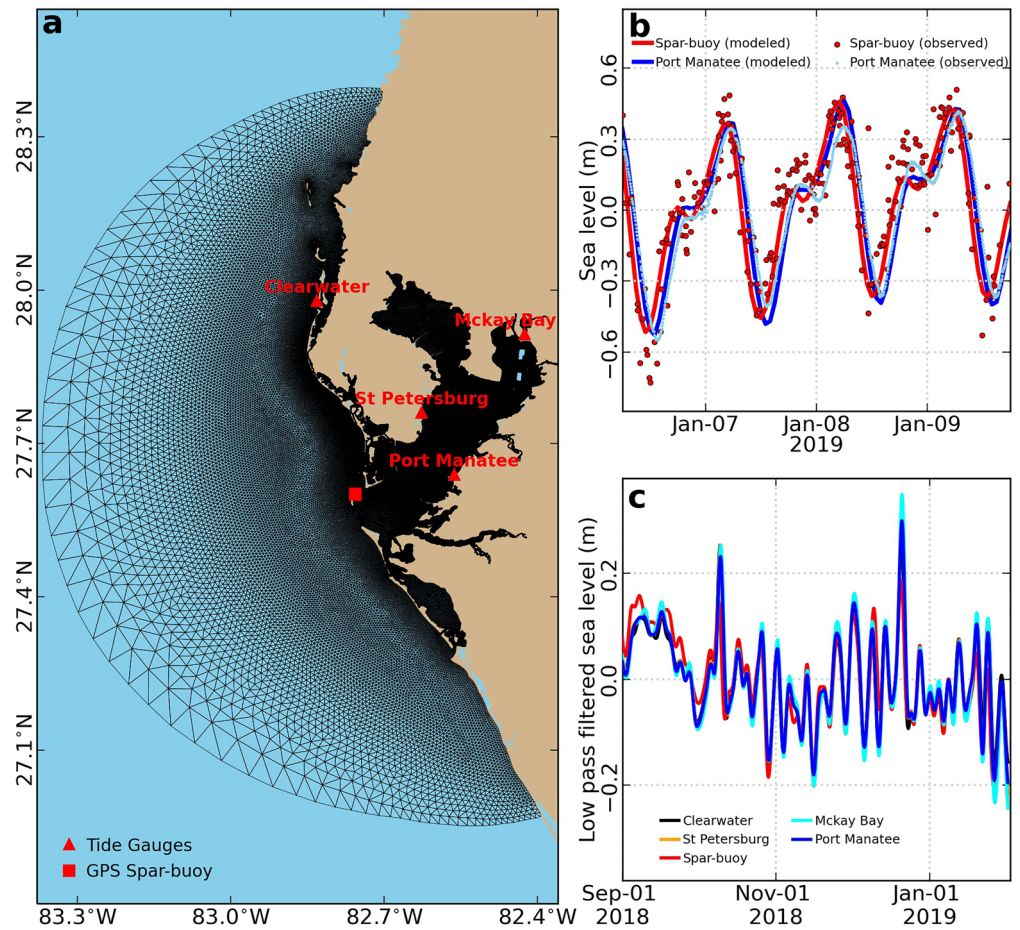


Figure 9. Sea levels modeled by the Tampa Bay Coastal Ocean Model (TBCOM). (a) Black mesh shows the model domain, red markers mark the Global Positioning System (GPS) spar-buoy and tide gauge locations. (b) 3.5-day example of observed and hourly modeled sea levels at the GPS spar-buoy and the Port Manatee tide gauge. (c) Differences between the low pass filtered observed and model simulated sea levels at the GPS spar-buoy and tide gauges before the adjustment. Details of the TBCOM modeling scheme are described in Chen (2021) and Chen et al. (2018, 2019).

and root mean square errors (RMSEs) between observed and TBCOM simulated sea levels at five different locations. By adjusting the simulated sea levels using the GPS spar-buoy-measured sea levels, the root mean square errors (RMSEs) between the observations and model simulations at all tide gauges were reduced by 19%–25%, and the correlation coefficients were increased by 4%–10%. These improvements are similar to

Table 1
Correlation Coefficient (CC) and Root Mean Square Error (RMSE) Between Observations and Tampa Bay Coastal Ocean Model (TBCOM) Simulations Before and After Adjustment by Water Levels Measured With a Tide Gauge at Port Manatee and the Global Positioning System (GPS) Spar-Buoy

Location	Before adjustment		Adjusted by Port Manatee		Adjusted by GPS spar-buoy	
	CC	RMSE (cm)	CC	RMSE (cm)	CC	RMSE (cm)
Clearwater	0.90	12.5	0.94	9.3	0.94	9.9
Mckay Bay	0.86	14.5	0.93	10.8	0.92	11.7
St Petersburg	0.86	13.0	0.94	9.1	0.93	9.9
Port Manatee	0.86	12.2	0.94	8.5	0.93	9.3
GPS spar-buoy	0.84	12.5	0.92	9.1	0.92	9.4

Note. Model domain, Global Positioning System (GPS) spar-buoy and tide gauge locations are shown in Figure 9a.

model adjustment using observations obtained by a tide gauge at Port Manatee (Table 1), implying that the GPS spar-buoy can be an alternative to conventional tide gauges for validation of the TBCOM.

For the diurnal to semi-diurnal tidal constituents, our TBCOM simulations clearly reveal a time lag of sea level variations at the GPS spar-buoy and the nearby tide gauge at Port Manatee (Figure 9b), consistent with the tidal harmonic analysis (Figure 6).

Under the current climate change scenario, Tampa Bay and many other densely populated coastal regions are becoming increasingly vulnerable to sea level rise and storm surge (Dixon, 2017; Vitousek et al., 2017). Better monitoring and modeling of coastal ocean waters provide valuable reference to policy makers and stakeholders for a city's flood risk and resilience assessment. Our GPS spar-buoy system can serve multiple purposes, is much cheaper to construct and deploy than rigid buoys, needs little maintenance, and can improve coastal ocean models.

5. Conclusions

An anchored GPS spar-buoy system, originally designed for measuring three-component seafloor motion in shallow water, is used to measure offshore sea levels in Tampa Bay by a combination of precise positioning and GPS interferometric reflectometry. Compared to a stationary GPS site on land, this system has broader sensing zones of the reflecting surface. For individual water level retrievals, agreement between the GPS spar-buoy and a nearby acoustic tide gauge is at ~15 cm level. Harmonic analyses of the water levels measured by the GPS spar-buoy and the nearby tide gauge suggest that the amplitude differences of major tidal constituents at the two locations are no more than 1.5 cm, while the largest short period tidal height variations (diurnal and semi-diurnal) at the tide gauge lag behind the spar-buoy site by ~1.5 hr. During a 2.9-year period, RMS of the de-tided daily mean sea level differences measured by the GPS spar-buoy and the closest tide gauge is 4.4 cm. Numerical modeling of ocean circulation throughout Tampa Bay suggests that including offshore sea levels measured by the GPS spar-buoy helps the model correct low-frequency sea level error propagated from the open boundary. The capabilities of measuring both seafloor motion and sea level change make the anchored GPS spar-buoy a comprehensive monitoring system for coastal waters.

Data Availability Statement

Water levels measured by the tide gauges at Port Manatee and St Petersburg (NOAA station IDs: 8726384 and 8726520) were downloaded from NOAA Tides and Currents (<https://tidesandcurrents.noaa.gov/water-levels.html?id=8726384> and <https://tidesandcurrents.noaa.gov/waterlevels.html?id=8726520>, last access on 5 September 2021). GPS data are archived at UNAVCO (<https://doi.org/10.7283/TM3V-P845>).

References

- Barnard, P. L., Short, A. D., Harley, M. D., Splinter, K. D., Vitousek, S., Turner, I. L., et al. (2015). Coastal vulnerability across the Pacific dominated by El Niño/Southern oscillation. *Nature Geoscience*, 8(10), 801–807. <https://doi.org/10.1038/ngeo2539>
- Bevis, M., Businger, S., Herring, T. A., Rocken, C., Anthes, R. A., & Ware, R. H. (1992). GPS meteorology: Remote sensing of atmospheric water vapor using the Global Positioning System. *Journal of Geophysical Research*, 97(D14), 15787–15801. <https://doi.org/10.1029/92jd01517>
- Chassignet, E. P., Hurlburt, H. E., Metzger, E. J., Smedstad, O. M., Cummings, J., Halliwell, G. R., et al. (2009). U.S. GODAE: Global ocean prediction with the HYbrid coordinate. *Ocean Model (HYCOM) Oceanography*, 22, 48–59. <https://doi.org/10.5670/oceanog.2009.39>
- Chen, C. S., Liu, H., & Beardsley, R. C. (2003). An unstructured, finite-volume, three-dimensional, primitive equation ocean model: Application to coastal ocean and estuaries. *Journal of Atmospheric and Oceanic Technology*, 20, 159–186. [https://doi.org/10.1175/1520-0426\(2003\)020<0159:augfvt>2.0.co;2](https://doi.org/10.1175/1520-0426(2003)020<0159:augfvt>2.0.co;2)
- Chen, J. (2021). *On the physical oceanography of Tampa Bay (Ph.D. Diss.)*. University of South Florida.
- Chen, J., Weisberg, R. H., Liu, Y., & Zheng, L. (2018). The Tampa Bay coastal ocean model performance for Hurricane Irma. *Marine Technology Society Journal*, 52(3), 33–42. <https://doi.org/10.4031/mts.j.52.3.6>
- Chen, J., Weisberg, R. H., Liu, Y., Zheng, L., & Zhu, J. (2019). On the momentum balance of Tampa Bay. *Journal of Geophysical Research: Oceans*, 124, 4492–4510. <https://doi.org/10.1029/2018jc014890>
- Dixon, T. H. (1991). An introduction to the global positioning system and some geological applications. *Reviews of Geophysics*, 29(2), 249–276. <https://doi.org/10.1029/91rg00152>
- Dixon, T. H. (2017). *Curbing catastrophe: Natural hazards and risk reduction in the modern world*. Cambridge University Press.
- Egbert, G. D., & Erofeeva, S. Y. (2002). Efficient inverse modeling of barotropic ocean tides. *Journal of Atmospheric and Oceanic Technology*, 19(2), 183–204. [https://doi.org/10.1175/1520-0426\(2002\)019<0183:eimobo>2.0.co;2](https://doi.org/10.1175/1520-0426(2002)019<0183:eimobo>2.0.co;2)

Acknowledgments

S. Xie is supported by the Scripps Postdoctoral Scholar Award. Development of the GPS spar-buoy system was funded by U.S. NSF-OTIC grant 1538179 to T. H. Dixon. This research was supported in part through a cooperative agreement between NOAA's Office of Coast Survey and the University of South Florida through the Center for Ocean Mapping and Innovative Technologies (COMIT), NA20NOS4000227. The authors acknowledge technical support by Jason Law at the USF-CMS Ocean Circulation Group and Chad Lembke and Randy Russell at the USF-CMS Center for Ocean Technology. T. Tide was used for harmonic analyses (Pawlowicz et al., 2002). Two anonymous reviewers are acknowledged for constructive comments on the paper.

- Hallegette, S., Green, C., Nicholls, R. J., & Corfee-Morlot, J. (2013). Future flood losses in major coastal cities. *Nature Climate Change*, 3(9), 802–806. <https://doi.org/10.1038/nclimate1979>
- He, R., Liu, Y., & Weisberg, R. H. (2004). Coastal ocean wind fields gauged against the performance of a coastal ocean circulation model. *Geophysical Research Letters*, 31, L14303. <https://doi.org/10.1029/2003GL019261>
- Ho, C. M., Mannucci, A. J., Lindqwister, U. J., Pi, X., & Tsurutani, B. T. (1996). Global ionosphere perturbations monitored by the worldwide GPS network. *Geophysical Research Letters*, 23(22), 3219–3222. <https://doi.org/10.1029/96gl02763>
- International Altimetry Team. (2021). Altimetry for the future: Building on 25 years of progress. *Advances in Space Research*, 68. <https://doi.org/10.1016/j.asr.2021.01.022>
- Karegar, M. A., Larson, K. M., Kusche, J., & Dixon, T. H. (2020). Novel quantification of shallow sediment compaction by GPS interferometric reflectometry and implications for flood susceptibility. *Geophysical Research Letters*, 47(14), e2020GL087807. <https://doi.org/10.1029/2020gl087807>
- Landskron, D., & Böhm, J. (2018). VMF3/GPT3: Refined discrete and empirical troposphere mapping functions. *Journal of Geodynamics*, 92, 349–360. <https://doi.org/10.1007/s00190-017-1066-2>
- Larson, K. M. (2013). A new way to detect volcanic plumes. *Geophysical Research Letters*, 40(11), 2657–2660. <https://doi.org/10.1002/grl.50556>
- Larson, K. M., Lay, T., Yamazaki, Y., Cheung, K. F., Ye, L., Williams, S. D., & Davis, J. L. (2021). Dynamic sea level variation from GNSS: 2020 Shumagin Earthquake tsunami resonance and hurricane Laura. *Geophysical Research Letters*, 48, e2020GL091378. <https://doi.org/10.1029/2020GL091378>
- Larson, K. M., & Nievinski, F. G. (2013). GPS snow sensing: Results from the EarthScope plate boundary observatory. *GPS Solutions*, 17(1), 41–52. <https://doi.org/10.1007/s10291-012-0259-7>
- Larson, K. M., Ray, R. D., Nievinski, F. G., & Freymueller, J. T. (2013). The accidental tide gauge: A GPS reflection case study from Kachemak Bay, Alaska. *IEEE Geoscience and Remote Sensing Letters*, 10(5), 1200–1204. <https://doi.org/10.1109/lgrs.2012.2236075>
- Larson, K. M., Ray, R. D., & Williams, S. D. (2017). A 10-year comparison of water levels measured with a geodetic GPS receiver versus a conventional tide gauge. *Journal of Atmospheric and Oceanic Technology*, 34(2), 295–307. <https://doi.org/10.1175/jtech-d-16-0101.1>
- Liu, L., & Larson, K. M. (2018). Decadal changes of surface elevation over permafrost area estimated using reflected GPS signals. *The Cryosphere*, 12(2). <https://doi.org/10.5194/tc-12-477-2018>
- Löfgren, J. S., & Haas, R. (2014). Sea level measurements using multi-frequency GPS and GLONASS observations. *EURASIP Journal on Applied Signal Processing*, 2014(1), 1–13. <https://doi.org/10.1186/1687-6180-2014-50>
- Mayer, D. A., Weisberg, R. H., Zheng, L., & Liu, Y. (2017). Winds on the West Florida Shelf: Regional comparisons between observations and model estimates. *Journal of Geophysical Research: Oceans*, 122(2), 834–846. <https://doi.org/10.1002/2016JC012112>
- Miguez, B. M., Testut, L., & Wöppelmann, G. (2012). Performance of modern tide gauges: Towards mm-level accuracy. *Scientia Marina*, 76(S1), 221–228. <https://doi.org/10.3989/scimar.03618.18a>
- Pawlowicz, R., Beardsley, B., & Lentz, S. (2002). Classical tidal harmonic analysis including error estimates in MATLAB using T_TIDE. *Computers & Geosciences*, 28, 929–937. [https://doi.org/10.1016/s0098-3004\(02\)00013-4](https://doi.org/10.1016/s0098-3004(02)00013-4)
- Peng, D., Hill, E. M., Li, L., Switzer, A. D., & Larson, K. M. (2019). Application of GNSS interferometric reflectometry for detecting storm surges. *GPS Solutions*, 23(2), 47. <https://doi.org/10.1007/s10291-019-0838-y>
- Peng, F., & Deng, X. (2020). Validation of Sentinel-3A SAR mode sea level anomalies around the Australian coastal region. *Remote Sensing of Environment*, 237, 111548. <https://doi.org/10.1016/j.rse.2019.111548>
- Purnell, D., Gomez, N., Chan, N. H., Strandberg, J., Holland, D. M., & Hobiger, T. (2020). Quantifying the uncertainty in ground-based GNSS-reflectometry sea level measurements. *IEEE Journal of Selected Topics in Applied Earth Observations and Remote Sensing*, 13, 4419–4428. <https://doi.org/10.1109/jstars.2020.3010413>
- Roesler, C., & Larson, K. M. (2018). Software tools for GNSS interferometric reflectometry (GNSS-IR). *GPS Solutions*, 22(3), 1–10. <https://doi.org/10.1007/s10291-018-0744-8>
- Roggenbuck, O., & Reinking, J. (2019). Sea surface heights retrieval from ship-based measurements assisted by GNSS signal reflections. *Marine Geodesy*, 42(1), 1–24. <https://doi.org/10.1080/01490419.2018.1543220>
- Vitousek, S., Barnard, P. L., Fletcher, C. H., Frazer, N., Erikson, L., & Storlazzi, C. D. (2017). Doubling of coastal flooding frequency within decades due to sea-level rise. *Scientific Reports*, 7(1), 1–9. <https://doi.org/10.1038/s41598-017-01362-7>
- Wang, X., Zhang, S., Wang, L., He, X., & Zhang, Q. (2020). Analysis and combination of multi-GNSS snow depth retrievals in multipath reflectometry. *GPS Solutions*, 24, 1–13. <https://doi.org/10.1007/s10291-020-00990-3>
- Watson, C., Coleman, R., & Handsworth, R. (2008). Coastal tide gauge calibration: A case study at Macquarie Island using GPS buoy techniques. *Journal of Coastal Research*, 24(4244), 1071–1079. <https://doi.org/10.2112/07-0844.1>
- Weisberg, R. H., & Zheng, L. (2006). Circulation of Tampa Bay driven by buoyancy, tides, and winds, as simulated using a finite volume coastal ocean model. *Journal of Geophysical Research*, 111(C1). <https://doi.org/10.1029/2005jc003067>
- Weisberg, R. H., Zheng, L., & Peebles, E. (2014). Gag grouper larvae pathways on the West Florida Shelf. *Continental Shelf Research*, 34, 11–23. <https://doi.org/10.1016/j.csr.2014.06.003>
- Williams, S. D. P., & Nievinski, F. G. (2017). Tropospheric delays in ground-based GNSS multipath reflectometry—Experimental evidence from coastal sites. *Journal of Geophysical Research: Solid Earth*, 122(3), 2310–2327. <https://doi.org/10.1002/2016jb013612>
- Xie, S., Law, J., Russell, R., Dixon, T. H., Lembke, C., Malservisi, R., et al. (2019). Seafloor geodesy in shallow water with GPS on an anchored spar buoy. *Journal of Geophysical Research: Solid Earth*, 124(11), 12116–12140. <https://doi.org/10.1029/2019jb018242>
- Zhang, S., E. D., Wang, Z., Li, Y., Jin, B., & Zhou, C. (2008). Ice velocity from static GPS observations along the transect from Zhongshan station to Dome A, East Antarctica. *Annals of Glaciology*, 48, 113–118
- Zheng, L., & Weisberg, R. H. (2012). Modeling the west Florida coastal ocean by downscaling from the deep ocean, across the continental shelf and into the estuaries. *Ocean Modelling*, 48, 10–29. <https://doi.org/10.1016/j.ocemod.2012.02.002>
- Zhu, J., Weisberg, R. H., Zheng, L., & Han, S. (2015). Influences of channel deepening and widening on the tidal and nontidal circulations of Tampa Bay. *Estuaries and Coasts*, 38(1), 132–150. <https://doi.org/10.1007/s12237-014-9815-4>